21st-century snowfall and snowpack changes over the Southern California mountains

Fengpeng Sun, Alex Hall, Marla Schwartz, Daniel Walton, Neil Berg
Department of Atmospheric and Oceanic Sciences, UCLA

Corresponding author address: Fengpeng Sun, Department of Atmospheric and Oceanic Sciences, University of California, Los Angeles.
E-mail: sun@atmos.ucla.edu

Abstract

We project future snowfall and snowpack changes over the mountains of Southern California using a new hybrid dynamical-statistical framework. Output from all general circulation models (GCMs) in phase 5 of the Coupled Model Intercomparison Project archive is downscaled to 2-km resolution over the region. Variables pertaining to snow are analyzed for the middle (2041–2060) and end (2081–2100) of the 21st century under two Representative Concentration Pathways (RCPs) scenarios: RCP8.5 ("business-as-usual") and RCP2.6 ("mitigation"). These four sets of projections are compared with a baseline reconstruction of climate from 1981 to 2000. For both future time slices and scenarios, ensemble-mean total winter snowfall loss is widespread. By mid-21st-century under RCP8.5, ensemble-mean winter snowfall is about 70% of baseline, whereas the corresponding value for RCP2.6 is somewhat higher (about 80% of baseline). By end-of-century, however, the two scenarios diverge significantly. Under RCP8.5, snowfall sees a dramatic further decline; 2081–2100 totals are only about half of baseline totals. Under RCP2.6, only a negligible further reduction from mid-century snowfall totals is seen. Due to the spread in the GCM climate projections, these figures are all associated with large inter-model uncertainty. Snowpack on the ground, as represented by April 1st snow water equivalent is also assessed. Due to enhanced snowmelt, the loss seen in snowpack is generally 50% greater than that seen in winter snowfall. By mid-century under RCP8.5, warming-accelerated spring snowmelt leads to snow-free dates that are about one to three weeks earlier than in the baseline period.

1. Introduction

Streamflow from snowfall and snowpack in mountain regions is a key freshwater source for California. The natural reservoir that snow provides is a critical element of water supply management and flood control. Climate change poses challenges to California's water infrastructure through its large effects on snow. Higher surface temperatures due to increased greenhouse gas emissions will likely cause more precipitation to fall as rain instead of snow and lead to faster and earlier snow melt. The resulting snowpack loss is likely to mean less stream flow in late spring and early summer, and possibly more stream flow and more streamflow variability in winter. In addition to the implications for water supply management and flood control, this could have negative impacts on agriculture and recreational activities, as well as plant and wildlife ecology. Meanwhile, water demand is expected to increase due to a hotter climate and growing population. It is therefore critical to assess regional snowpack changes at space and time scales relevant for regional and local resource management decisions.

Many studies have documented observed changes in snow measures over the past several decades, and assessed impacts of global and regional warming on snow (e.g., Barnett et al. 2005; Knowles et al. 2006; Barnett et al. 2008; Pederson et al. 2011; Pierce and Cayan 2013). Several observational and numerical modeling studies have also investigated potential effects of warming on Sierra Nevada snowpack (e.g., Howat and Tulaczyk 2005; Mote et al. 2005; Mote 2006; Maurer 2007; Cayan et al. 2008; Kapnick and Hall 2010; Pavelsky et al. 2011) and other mountainous regions in the Western United States (Kim et al. 2002; Knowles and Cayan 2002; Leung and Qian 2003; Mote 2003; Leung et al. 2004; Snyder et al. 2004; Bales et al. 2006; Salathé et al. 2008; Minder

2010; Abatzoglou 2011; Kapnick and Hall 2012; Ashfaq et al. 2013; Klos et al. 2014). However, few studies have focused on snowfall and snowpack variability and change in Southern California mountains.

Climate change information is available from projections by general circulation models (GCMs), such as those archived in the Coupled Model Intercomparison Project Phase 5 (CMIP5; Taylor et al. 2012). However, the spatial scale of GCM output is far too coarse to provide accurate estimates of snow variability and projections for regional or local studies. GCMs poorly represent topography, even in the largest mountain ranges, minimizing topographic influences on circulation and hence rainfall and snowfall in mountain regions (Luce et al. 2013). This presents an issue in the study of climate change effects on snowpack because snowpack changes may vary by region and elevation. Whereas snowpack may decline in some areas, it could be less sensitive to warming in others, with no change or even increases where total precipitation is projected to increase. In addition to changes in mean snow quantities, changes in seasonality and timing of snowfall and snowmelt are expected. Understanding which areas of mountain ranges are most vulnerable to climate change is critical for regional and local climate assessments and water management planning. To address the limitations of coarse-resolution GCMs, dynamical and statistical techniques are commonly used to downscale GCM projections.

Dynamical downscaling employs a regional climate model with much higher spatial resolution than GCMs, while relying on GCMs for boundary information. Like GCMs, a regional climate model is based on fundamental physical laws governing the climate system. A high-resolution regional climate model can simulate regional- and local-scale climate variations, including orographic precipitation, rain shadows, and snow processes in mountainous regions. Dynamical downscaling has been widely applied over many regions (e.g., Leung and Ghan 1999; Giorgi et al. 2001; Wang et al. 2004; Chin 2008) and is valuable in providing information on regional climate change, including California (Cayan 1996; Cayan et al. 2001; Leung et al. 2003; Caldwell et al. 2009; Qian et al. 2009; Pan et al. 2011). Although dynamical downscaling probably provides the most physically realistic approach to downscaling low-resolution climate data and provides a comprehensive suite of climate variables, it is enormously computationally expensive.

Alternatively, statistical downscaling is computationally cheap. Statistical models are based on empirical relationships between known climate predictors and climate variables of interest at the regional scale. These relationships are presumed to hold true for the future and are used to project regional climate change given the change in the climate predictors (von Storch et al. 1993; Wilby et al. 2004). Statistical downscaling approaches have been applied to various regions of interest. Temperature and precipitation are the climate variables most commonly used in statistical downscaling studies (e.g., Hayhoe et al. 2004; Pierce et al. 2013). Snowfall and snowpack are statistically downscaled less often, in spite of their importance for hydroclimate.

To obtain reliable climate change information at the regional scale, this study develops and applies a novel hybrid dynamical-statistical framework. Unlike previous downscaling studies, which use either a dynamical or a statistical technique, this study combines both, developing statistical relationships directly from dynamically downscaled output. This study undertakes dynamical downscaling for a reanalysis-driven baseline simulation (1981–2000) and a small representative sample of GCMs forced by a "business-as-usual" greenhouse gas emissions scenario, i.e., Representative Concentration Pathway 8.5 (RCP8.5; Meinshausen et al. 2011) for a mid-21st-century time slice (2041–2060). A statistical model is then developed to reproduce the snowfall and snowpack variations in the baseline period using other climate variables (i.e., surface temperature and precipitation) as predictors. We confirm the accuracy of the statistical model by comparing its future projections to those of the dynamically downscaled mid-21st-century simulations. Finally, we apply the validated statistical model, using temperature and precipitation projections from previous studies (Walton et al. 2015; Sun et al. 2015; Berg et al. 2015), to project regional snowfall and snowpack changes for all the available GCMs.

Combining dynamical and statistical downscaling techniques in this way allows us to incorporate the most important dynamical processes shaping regional snowfall and snowpack variations and change without dynamically downscaling each GCM. The hybrid technique provides ensemble-mean estimates and quantifies uncertainties associated with differences across various GCM projections. This study marks the first time a full ensemble of GCM output has been downscaled to high-resolution regional scales to create both snowfall and snowpack projections. The hybrid framework also allows us to assess snowfall and snowpack changes associated with different emissions scenarios and time periods: We downscale the available GCMs for the mid-21st-century and end-of-21st-century (2081–2100) periods under both "business-as-usual" RCP8.5 scenario and "mitigation" RCP 2.6 scenario, in which greenhouse gas emissions are aggressively reduced in the coming decades.

The paper is organized as follows: Section 2 describes the dynamical downscaling experiment design and evaluation. Section 3 describes the statistical downscaling framework and its performance in baseline prediction. Section 4 presents the evaluation of performance of statistical downscaling under future climate change. Section 5 presents the future snowfall and April 1st snow water equivalent (SWE) changes, followed by comparison and discussion of sensitivities to choice of greenhouse gas emissions scenario. Major findings are summarized and discussed in Section 6.

2. Dynamical Downscaling

a. Experimental Design

Dynamical downscaling simulations are performed using the Weather Research and Forecasting Model (WRF; Skamarock et al. 2008) version 3.2. WRF is a community mesoscale model developed by the National Center for Atmospheric Research (NCAR). It is designed for use on regional grids for a range of applications, including weather forecasts and climate simulations. WRF consists of a fully compressible nonhydrostatic dynamical core with high-order, conserving numerical techniques, and a full suite of physics parameterizations. Sensitivity experiments using various combinations of parameterizations are performed to find an optimal WRF configuration for realistically simulating Southern California climate and its variability. The following parameterization schemes are chosen: Kain-Fritsch (new Eta) cumulus (Kain 2004), Yonsei University boundary layer (Hong et al. 2006), Purdue Lin microphysics (Lin et al. 1983), Rapid Radiative Transfer Model longwave radiation (Mlawer et al. 1997), and Dudhia shortwave radiation (Dudhia 1989). We use the Noah land surface model (Chen and

Dudhia 2001) to simulate land surface processes including vegetation, soil, snowpack, and exchange of energy, momentum, and moisture between the land and atmosphere.

We use three nested domains (18, 6, and 2 km) to reach a high enough resolution to represent the region's topography and coastlines (refer to Fig. 1 in Walton et al. 2015). The outermost domain, at 18-km resolution, covers the entire state of California and the adjacent ocean. The middle domain (6-km) covers roughly the southern half of California, including the southern Sierra Nevada. The innermost domain (2-km) encompasses the greater Los Angeles region and its surrounding mountains. In each domain, all variables within five grid cells from the horizontal lateral boundary are relaxed towards the corresponding values at the boundaries. This procedure ensures smooth transitions across these boundaries. Each domain has 43 sigma-levels in the vertical. To provide a better representation of surface and boundary layer processes, the model's vertical resolution is enhanced near the surface, with 30 sigma-levels below 3 km. Fig. 1 shows the topography for the innermost domain at its native 2-km resolution. The main features of both the topography and coastlines are represented well at this resolution.

Using this model configuration, we first perform a reanalysis-driven "baseline" simulation (1981–2000) whose purpose is three-fold: (1) to evaluate the model's ability to simulate regional climate, (2) to provide a baseline climate state against which a future climate simulation can be compared, and (3) to build the statistical relationships in the statistical downscaling framework (section 3a). For the baseline simulation, WRF is forced along the boundaries of the outermost domain by the National Centers for Environmental Prediction's 3-hourly North American Regional Reanalysis (NARR;

Mesinger et al. 2006) for the 1981–2000 period. Using the same model configuration, we then perform a series of dynamical downscaling experiments to simulate future climate associated with five CMIP5 GCMs for the mid-century period under the RCP8.5 forcing scenario. The selected GCMs are the NCAR Community Climate System Model, Version 4 (CCSM4; Gent et al. 2011), the Centre National de Recherches Meteorologiques Climate Model 5 (CNRM-CM5; Voldoire et al. 2012), the NOAA Geophysical Fluid Dynamics Laboratory Climate Model 3 (GFDL-CM3; Donner et al. 2012), the AORI (U. Tokyo), NIES, and JAMSTEC Atmospheric Chemistry Coupled MIROC Earth System Model (MIROC-ESM-CHEM; Watanabe et al. 2011), and Max Planck Institute for Meteorology Low Resolution Earth System Model (MPI-ESM-LR; Brovkin et al. 2013).

To produce future climate boundary conditions for the WRF simulations, we first quantify the differences in GCM monthly climatology between the mid-century (2041–2060) and baseline (1981–2000) periods. Monthly differences are calculated for three-dimensional variables, including temperature, relative humidity, zonal and meridional winds, and geopotential height, and two-dimensional surface variables, including surface temperature, relative humidity, winds, and pressure). On a monthly varying basis, we add these climate change signals to the NARR reanalysis data corresponding to the baseline period. Thus, we perturb the NARR baseline boundary conditions (1981–2000) with monthly-averaged climate change signals between the mid-century and baseline (2041–2060 minus 1981–2000) provided by each GCM. These perturbed NARR data are then used as boundary conditions for the outermost domain of the regional model. This technique has been previously used to downscale GCM signals to fine spatial scales for other regions (e.g., Schär et al. 1996; Sato et al. 2007; Hara et al. 2008; Knutsen et al.

2008; Kawase et al. 2009; Lauer et al. 2010; Seo and Xie 2011; Rasmussen et al. 2011). Sun et al. (2015) addressed this perturbation approach's caveats and limitations, including the unchanged interannual variability and weather and transient signals on the model domain's boundaries. CO_2 levels are also increased in WRF to match the changes in CO_2-equivalent radiative forcing in the RCP8.5 scenario averaged over the mid-century period compared to the baseline.

Computational limitations do not allow us perform full 20-year dynamical downscaling simulations for each of the five GCMs for the mid-21st-century period. So we first perform a 20-year (2041–2060) dynamically downscaling of climate change signals in CCSM4. Because we perturb each year in the future 20-year period with the same monthly-varying climate change signals from CCSM4, we expect the climate change patterns for each year to be similar. In fact, any four-year period within the full 20-year period captures the snow change and other climate change signals found in the full 20-year period of CCSM4 downscaling very well (not shown). Therefore, we dynamically downscale the other four GCMs for only four years. In each simulation, the perturbed boundary conditions are created by adding the 20-year GCM climate change signal (2041–2060 values minus 1981–2000 values) to the 1997–2000 NARR data.

b. Model Evaluation

Fig. 2 presents the dynamically downscaled spatial distributions of the baseline (1981–2000) snowfall climatology over the Los Angeles region from November through April. Winter months December, January, February, and March (DJFM) have the greatest snowfall for most areas, and have the largest spatial extent of snowfall. DJFM snowfall accounts for more than 80% of annual accumulated snowfall across the region. Snowfall is mainly found in mountain regions, at elevations of 1500 meters and higher. Snowfall generally increases with elevation, with larger amounts on the coastward-facing side of the ranges. Climatological snowfall is negligible (less than 1mm per month) at high-elevation desert regions (e.g., the Mojave Desert). Such a tiny amount of snowfall would probably not survive long enough on the ground to lead to any substantial accumulation, especially when the surface temperature is not cold enough. Snowfall greater than 200 mm per month is seen in high-elevation mountain regions (2000 meters and higher), including the southern rim of the Sierra Nevada and the Tehachapi, San Emigdio, San Gabriel, San Bernardino, and San Jacinto Mountains (refer to Fig. 1 for mountain locations). At the highest elevations, monthly accumulated snowfall can reach 300 mm per month in the peak season.

The dynamical model's ability to reproduce snowfall climatology and its temporal and spatial variations are assessed by comparing output from the 2-km baseline climate simulation to available observational measurements. Quality-controlled daily snowfall, precipitation, and maximum temperature data are obtained from the Western Regional Climate Center (WRCC), which collects daily data from the National Weather Service (NWS) Cooperative Observer Program (COOP).

Data from each NWS-COOP station within the 2-km WRF domain are evaluated, and stations with no recorded snowfall are excluded. From the remaining stations, we select those with daily snowfall and temperature measurements for at least 75% of the baseline period, which allows for the assessment of both climatology and interannual variability. Four NWS-COOP stations met these criteria: Big Bear Lake and Lake

Arrowhead in the San Bernardino Mountains, Idyllwild in the San Jacinto Mountains, and Tehachapi in the Tehachapi Mountains. Table 1 summarizes the identifying information associated with each observational station, including COOP ID, location, elevation, and period of available data. All four stations are in mountain regions and represent a variety of elevations ranging from 1224 m to 2070 m. At the four stations, individual months with more than 5 missing days of data are not used for monthly statistics and are not included in annual totals for that year.

There are several barriers to comparing observed and simulated snowfall data in a straightforward way. First, the model grid cells in the vicinity of a measurement station may not be at the exact elevation as the measurement station. Because of the strong dependence of snowfall on elevation, this can lead to a slight mismatch between observed and simulated data. To minimize this issue, we consider the four model grid cells nearest each station and select the one whose elevation is in closest agreement with that of the station.

Second, a direct comparison of snowfall water equivalent (SFE) by WRF to that of observed snowfall is not possible due to an absence of *in situ* liquid water equivalent of snowfall measurements in the study area for the baseline period. To compare WRF-simulated SFE to fresh snowfall observations at NWS-COOP stations, we convert the observed depth of fresh snowfall to its water equivalent using the following relationship:

$$SFE = snowfall_{depth} \times \rho_{snow} / \rho_{water} \tag{1}$$

The density of freshly fallen snow is not directly measured. However, total daily precipitation is available. We use the above equation to estimate density of freshly fallen snowfall at each NWS-COOP station. SFE is taken to be the observed daily precipitation value on days with nonzero snowfall and maximum temperatures less than or equal to 0ºC. We exclude days with nonzero snowfall and maximum temperatures above 0ºC, as some of the measured precipitation on those days is likely to have been in the form of rain. Across the four stations, estimated snow densities range from 63 to 129 kg/m3, well within the range of previous studies. These studies found that snow density varies from 10 to 500 kg/m3 depending on location, meteorological condition, crystal size, crystal shape, degree of riming, and other snow metamorphosis processes (Pomeroy and Brun 2001; Roebber et al. 2003; Baxter et al. 2005; Kay 2006). Our estimated snow densities are also comparable to the most commonly observed values, between 60 and 100 kg/m3, suggested by Judson and Doesken (2000). Using our calculation of observed snowfall density, we are able to estimate the observed SFE using equation (1), and then compare the estimate to simulated snowfall at the selected model grid cells.

We now present model evaluation results, focusing on the climatological seasonal cycle and interannual variability. Figure 3a compares monthly climatological simulated snowfall values (i.e., SFE) to observations. WRF's seasonal cycle of snowfall is consistent with observations for each of the four stations, as the simulated and observed values are very well-correlated, with an average correlation coefficient of 0.96 across the sites. The model also accurately simulates spatial variations in climatological snowfall. The root-mean-square error of all data points in Fig. 3a is 4 mm. A large fraction of this error has to be due to the unavoidable assumption of constant snow density. Fig. 3b compares annual accumulated snowfall (from September to August of the following year) between each NWS-COOP station and the corresponding WRF grid cell for all years in the baseline period with available data. For each station, the simulated and observed values are significantly correlated, with an average correlation of 0.59. The overall correlation of the data points in Fig. 3b is 0.76, providing a combined evaluation of the spatial and interannual snowfall variability. The fact that this number is higher than the correlation associated with any individual station is an indication that the model captures spatial variability somewhat better than temporal variability. Again, the assumption of constant snow density probably contributes significantly to the model-observation discrepancies in Fig. 3b.

Overall, Fig. 3 shows that our WRF framework simulates the temporal and spatial variations of snowfall during the baseline period with reasonable accuracy at specific mountain locations where reliable observational data are available. Based on this evidence, it is very likely that the model is able to reproduce the temporal and spatial snowfall variations across the whole domain, even at very high elevations where there is certainly substantial snowfall but observations are sparse or unavailable.

3. Statistical Downscaling

In this section, we present the statistical framework to reproduce snowfall and snowpack variations. The framework is based on the multiple linear regression analysis between interannual variations in snow properties and climate variables from the reanalysis-driven, dynamically downscaled baseline simulation.

a. Snowfall Model

Precipitation and temperature are key factors affecting snowfall. The relationship between precipitation and snowfall estimates is fairly straightforward. In the Noah land surface model, precipitation phase is determined by a simple partitioning scheme based on estimated surface air temperatures. (Note: both surface air temperature and surface skin temperature are used in the analysis, and they produce similar results.) Temperatures below the freezing point of water are assumed to result in precipitation that is 100% snowfall, and those above are assumed to result in 100% rainfall.

Snowfall is highly sensitive to elevation and season. To create the statistical framework, we first bin all elevations in 100-meter increments. Then, for all grid cells within each bin, we average variables for each month. Fig. 4 shows a vector representation of interannual correlations between snowfall and precipitation (x-direction) as well as snowfall and temperature (y-direction) in each elevation bin and winter month (DJFM) in the baseline period. Nearly all elevation bins (except for very low elevations) show significant positive correlations (rightward direction) between precipitation and snowfall in each of the winter months. This is expected, as precipitation places a fundamental limit on how much snowfall out of total precipitation is possible, and is determinative of snowfall at elevations above the freezing line. At some low and moderate elevations, temperature plays the stronger role. For instance, the correlation between snowfall and temperature is as large as 0.83 around 1800 m in February. At these low and moderate elevations, regional warming in the absence of precipitation changes would result in snowfall declines. In contrast, at high elevations, because temperatures remain below the freezing point, temperature fluctuations have less impact on precipitation phase. The highest elevations might be also susceptible to warming, but most are so cold that the warmth of a particular winter has only a small effect on snowfall and snowpack.

We next explore how well WRF-simulated interannual variability in monthly accumulated snowfall is represented using monthly averaged temperature and accumulated precipitation. To do this, we use the following multiple linear regression equation:

$$\hat{S}(T,P) = \max\,[\,\alpha * T + \beta * P + \gamma,\ 0] \qquad (2)$$

where α and β are the regression coefficients for monthly averaged temperature (T) and monthly accumulated precipitation (P), respectively, and γ is the residual term. $\hat{S}$ represents the monthly accumulated snowfall values associated with temperature and precipitation and is not allowed to be negative. As shown in Fig. 4, the sensitivity of snowfall to temperature and precipitation varies by elevation and month. We construct the best-fit multiple linear regression model for each winter month and elevation bin in the region, and apply this multiple linear regression model to the WRF-simulated baseline snowfall, temperature, and precipitation.

Using this regression model, a snowfall value for each winter month and each elevation bin can be predicted from WRF's temperature and precipitation values; this value can then be compared with WRF-simulated snowfall. Fig. 5 compares the regression-derived snowfall and WRF-simulated snowfall for three sample elevation bins in February. Fig. 5 suggests temperature and precipitation can predict the interannual variability of mountain snowfall with a high degree of success. For a high-elevation bin (2500–2600 m, Fig. 5a), the correlation coefficient between the regression-derived snowfall and WRF-simulated snowfall is 0.98. In this case, snowfall is determined almost entirely by total precipitation (see Fig. 4). For a mid-elevation bin (2000–2100 m, Fig. 5b), the correlation between the regression-derived snowfall and WRF-simulated snowfall is 0.93. For a relatively low-elevation bin (1500–1600 meters, Fig. 5c), the correlation drops to 0.82. This indicates the statistical model's quality declines somewhat as elevation decreases. Overall, Fig. 5 suggests snowfall derived from the multiple linear regression model represents the interannual variation at all elevations quite well.

b. SWE Model

As with snowfall, we build an analogous statistical framework for the snowpack on the ground (represented by SWE) using multiple linear regression analysis. SWE is the depth of water that would result if the entire snowpack were to melt instantaneously. April 1st SWE is commonly used to assess snowpack and its variability. It is the most frequent observation date and is extensively used for spring streamflow forecasting and analysis (Howat and Tulaczyk 2005; Mote et al. 2005), as it is an indicator of the interannual variation in snowpack.

The relationship between April 1st SWE and winter mean temperature is more complex than that between April 1st SWE and winter accumulated precipitation. Additionally, temperature affects SWE in a more complex way than it does snowfall, as it directly impacts snowmelt through convective heat transfer from the air to the snowpack. Temperature is also indirectly consequential for humidity and water vapor pressure, which both contribute to snow sublimation and snowmelt (Hamlet et al. 2005). Previous studies have assessed the contributions of temperature and precipitation to observed snowpack variations and trends (Serreze et al. 1999; Howat and Tulaczyk 2005; Mote et al. 2005; and Mote 2006). Informed by these studies, we predict April 1st SWE from mean temperature and accumulated precipitation during the preceding winter months (December through March), using the following multiple linear regression equation:

$$\hat{SWE}_{April1st}(T_{DJFM}, P_{DJFM}) = \max\,[\,\alpha * T_{DJFM} + \beta * P_{DJFM} + \gamma\,,\,0] \quad (3)$$

As with snowfall, SWE sensitivity to temperature and precipitation varies with elevation. So we construct the regression model for each elevation bin. A plot similar to Fig. 5 (not shown) reveals that the multiple linear regression model reproduces the interannual variations of WRF-simulated baseline April 1st SWE at all elevations as successfully as the model predicting snowfall.

The success of this statistical framework indicates that the interannual variability in regional snowfall and snowpack are well explained by summaries of monthly regional climate. This implies that day-to-day or event-to-event weather fluctuations might be of secondary importance.

4. Statistical Model Performance under Climate Change

To project future snowfall and SWE using the statistical framework, it is necessary to verify that the relationships between baseline snow properties and baseline temperature and precipitation hold in the future climate. In this section, we validate the statistical downscaling framework by comparing its predictions of future snowfall and SWE against output from the multiple dynamical downscaling future simulations described in Section 2a.

Fig. 6 shows the statistically downscaled mid-21st-century seasonal cycles of snowfall under the RCP8.5 scenario (green), compared to the corresponding dynamically downscaled results for each future simulation (red) and the baseline simulation (black).

Data are shown for snowfall averaged over elevations above 1500 meters within the domain. There are significant snowfall declines at mid-century in all months for four of the five dynamical downscaling experiments. The only exception is the CNRM-CM5 simulation, which shows no change or even a slight increase in snowfall. This is the result of a projected precipitation increase for CNRM-CM5 (Berg et al. 2015), which apparently cancels out any snowfall reduction due to warming. The statistically downscaled results reproduce dynamically downscaled snowfall changes in each wet month with an error of less than 10%. The dynamical snowfall declines for CCSM4, GFDL-CM3, MIROC-ESM-CHEM, and MPI-ESM-LR are all generally well-captured by the statistical framework. The statistical model also reproduces snowfall's insensitivity to climate change in the CNRM-CM5 projection.

Fig. 7 compares statistically and dynamically downscaled results for winter (DJFM) accumulated snowfall as a function of elevation for all five experiments. The baseline snowfall is shown as a background reference (black). Dynamically downscaled results show snowfall reductions at all elevations for all experiments, with the exception of the very high elevations in CNRM-CM5. For each experiment, the statistical model tracks the dynamically downscaled results well at most elevations. For CCSM4, the statistical result reproduces the WRF-simulated snowfall almost perfectly in every elevation bin. For GFDL-CM3, CNRM-CM5, and MPI-ESM-LR, the statistical results overestimate overall snowfall, but the bias is generally less than 10%. It is noteworthy that above 2800 m, CNRM-CM5 simulates a snowfall increase, suggesting the stronger control is exerted by increased precipitation. This increase is captured in the statistically downscaled results as well. In general, the statistical model captures dynamically projected snowfall changes at all elevations in all five experiments with a reasonable degree of accuracy.

Next we evaluate the statistical model's ability to estimate April 1st SWE. Fig. 8 compares statistically and dynamically downscaled results for April 1st SWE as a function of elevation for all five experiments. For each GCM, the statistical SWE estimate generally matches dynamically downscaled SWE, with less than 10% error. The dwindling of snowpack on or even before April 1st at low and moderate elevations in GFDL-CM3 and MIROC-ESM-CHEM underscores the dominant effect of regional warming at these elevations in these models. The statistical model captures this effect well. The statistical projections also capture the increased SWE at very high elevations for CNRM-CM5. Overall, Figs. 6, 7, and 8 demonstrate that the statistical framework based on baseline relationships can be used to project future snowfall and SWE.

5. Projections for all GCMs

In this section, we estimate future winter snowfall and April 1st SWE using the aforementioned statistical framework, which efficiently approximates snow changes that would have been produced had dynamical downscaling been performed on all available GCMs (Table 2). We then assess the sensitivity of snow outcomes to emissions scenario.

a. Snowfall Projection

Two future time slices under the RCP8.5 emissions scenario are chosen for comparison: mid-21st-century (2041–2060) and end-of-21st-century (2081–2100). Statistical model predictors—temperature and precipitation—are taken from Walton et al.

(2015), Sun et al. (2015), and Berg et al. (2015), who developed hybrid dynamical-statistical downscaling approaches to project surface air temperature and precipitation changes for the two future time slices. These studies downscaled available CMIP5 GCMs and estimated the ensemble-mean as well as the associated intermodel range of future surface warming and precipitation changes in the greater Los Angeles region. Their main findings include warming at mid-century and continued warming at end-of-century, although the warming amplitude varies significantly across the region and GCMs (Walton et al. 2015; Sun et al. 2015). Winter precipitation projections vary in both sign and amplitude across models. Some GCMs project moistening, and others project drying in the region. But overall precipitation signals are weak, yielding no significant ensemble-mean precipitation change (Berg et al. 2015). With these studies' temperature and precipitation projections for each GCM as inputs, we use the snowfall statistical model to downscale and quantify snowfall changes in the region.

Fig. 9a and 9b present CMIP5 ensemble statistically downscaled DJFM accumulated snowfall, as a function of elevation, for the mid-21st-century and end-of-21st-century, respectively, under RCP8.5. Projected snowfall is shown as a percentage of the baseline snowfall. DJFM snowfall accounts for more than 80% of annual accumulated snowfall for the region. Under RCP8.5, the ensemble-mean shows a snowfall loss everywhere. Low elevations have the greatest reductions in snowfall, with less than 50% of baseline snowfall remaining on average. At lower elevations, surface air temperatures during precipitation events are more likely to breach the freezing point of water as the climate warms. Hence, a snow event is more likely to be converted to a rain event. Mid-elevation (2000–2500 m) snowfall is somewhat less sensitive to climate change, retaining about 70% of baseline snowfall in the ensemble-mean. High-elevation snowfall is projected to be relatively resilient, with roughly 90% of baseline snowfall remaining. Below 2400 m, every GCM projects a snowfall decline compared to the baseline under RCP8.5. At the highest elevations (above 3100 m), about two-thirds of the GCMs predict snowfall loss. High-elevation snowfall is relatively insensitive to warming because of the insensitivity of snowfall to temperature fluctuations (see Fig. 4) and is instead dominated by the precipitation change. The GCMs showing increased snowfall above 3100 m are those with a projected increase in total precipitation. Fig. 9a also shows the spread across GCM projections for each elevation bin. The spread is substantial across GCMs at each elevation, roughly 50–60 percentage points. For example, at the highest elevations, projected snowfall percentages range from about 70% to 120%. This range, which can be taken as a measure of uncertainty, is nearly half the ensemble-mean projection (about 95%).

End-of-21st-century snowfall under RCP8.5 (Fig. 9b) shows a further reduction from mid-century values at every elevation. Only about a quarter of GCM projections show a snowfall increase at the highest elevations. Ensemble-mean end-of-century snowfall is less than 20% of baseline snowfall at elevations below 1800 meters, about 50% at moderate elevations, and about 80% at high elevations. Model spread becomes somewhat smaller at end-of-century (40%) than at mid-century (50%). The greater consistency among GCMs at end-of-century may be due to the increasing magnitude of the temperature signal in all models, and its increasingly powerful effect on snowfall reduction.

b. SWE Projection

We next apply the statistical framework for April 1st SWE. Fig. 9c and 9d present the CMIP5 statistically downscaled April 1st SWE, as a function of elevation, for the mid-21st-century and end-of-21st century, respectively, under RCP8.5. Ensemble-mean April 1st SWE decreases at all elevations for both time periods. In general, higher elevations have more remaining snowpack, in accordance with elevation-dependent snowfall projections. As shown in Fig. 9c, every GCM projects snowpack reduction below 2400 m at mid-century, while above 2400 m, about one-tenth to one-third of the downscaled GCMs project increased snowpack. At very high elevations, ensemble-mean mid-century remaining snowpack is about 90% of baseline snowpack, similar to the ensemble-mean snowfall projections. Regional warming does not cause the temperature to breach the freezing point of water at very high elevations, so its impact on snow ablation and snowmelt spreads across GCM projections is minimal.

In contrast, at low and moderate elevations, the percentage of SWE lost is substantially larger than that of snowfall. Fig. 10 shows the ensemble-mean percentages of April 1st SWE compared to those of winter snowfall for the three sampled elevations. The remaining SWE percentage is as low as 26% at low elevations and about 54% at moderate elevations, while the corresponding snowfall percentage is nearly 48% and 71% at low and moderate elevations, respectively. Thus April 1st SWE is reduced by an additional 20 percentage points from the already-reduced winter snowfall. This suggests that in addition to its impacts on snowfall loss, warming plays a further role in enhancing ablation and melting of snow at low to moderate elevations. In all models, warming is large enough either to exaggerate the snow decline seen in models with reduced precipitation, or overcome any snow accumulation increase in models with increased precipitation. Fig. 9c also shows that there is a significant spread in projections of mid-century SWE across the GCMs, particularly at moderate and high elevations. For example, at 2700 m, the SWE percentage ranges from about 35% of baseline to about 120% of baseline. Model spread is larger than that seen in snowfall projections shown in Fig. 9a, indicating that variations among GCMs in snow ablation and melting add to their variations in snow deposition.

At end-of-century under RCP8.5, April 1st SWE is further reduced from mid-century values at all elevations, including the very high elevations (Fig. 9d). This implies that further warming more than compensates for any precipitation increases. Moderate elevations see the largest further reduction of snowpack, and the uncertainty range across GCMs is generally smaller than at mid-century. At elevations lower than 1700 m, all GCMs project a complete disappearance of snowpack on or before April 1st by end-of-century. End-of-century April 1st SWE reduction is larger than that of snowfall, particularly at moderate elevations. Fig. 10 shows that whereas about 52% of baseline winter snowfall remains at the end-of-century for moderate elevations, only about 31% of the snowpack remains on April 1st, yielding an additional SWE reduction of 20 percentage points. This further demonstrates that warming at end-of-century significantly enhances snow ablation and melting processes. A rule of thumb is that roughly two-thirds of the April 1st SWE loss is due to snowfall reduction, while about one-third is due to enhanced melting.

c. Sensitivity to Choice of Emissions Scenario

To account for uncertainty associated with choice of future emissions scenario, we project mid-century and end-century winter snowfall and April 1st SWE for the CMIP5 ensemble under RCP2.6, which assumes greenhouse gas emissions peak around 2030 then decline substantially thereafter. Fig. 9 and Fig. 10 assess the sensitivities of snow changes to emissions scenario. The cross markers in Fig. 9 denote the ensemble-mean snowfall and April 1st SWE projections under RCP2.6 for the corresponding time period. The ensemble-mean projection of snowfall under RCP2.6 is greater than that under RCP8.5 at all elevations for mid-century, and for nearly all elevations for end-of-century. However, at mid-century, RCP2.6 shows only about 10 percentage points more snowfall in low- and mid-elevations than RCP8.5, and the difference between the two scenarios in higher elevations is minimal. End-of-century projections show a greater contrast between the two scenarios, especially in low and moderate elevations. For instance, at very low elevations, the difference is as large as about 40 percentage points. In contrast to RCP8.5, the RCP2.6 scenario sees a negligible snowfall change at end-of-century compared with mid-century. Similarly, the remaining snowpack on April 1st in RCP2.6 represents minimal change from mid-century to end-of-century at all elevations, leading to significant contrast at end-of-century between these two scenarios.

6. Summary and Discussion

In this study, we develop a hybrid dynamical-statistical downscaling technique to produce 2-km-resolution projections of future snowfall and snowpack changes in the mountains of Southern California at the middle and end of the 21st century. This new hybrid technique combines both dynamical and statistical downscaling and develops the statistical relationships directly from dynamically downscaled output. The first step is to perform a dynamical downscaling for a baseline simulation (1981–2000) and a representative sample of GCMs forced by the RCP8.5 emissions scenario for a mid-century time slice (2041–2060). A statistical model is then developed to reproduce the snowfall and snowpack variations in the baseline period using surface temperature and total precipitation as predictors. The accuracy of the statistical model is evaluated by comparing its predictions to those of the dynamically downscaled baseline and mid-century simulations. Using surface temperature and precipitation projections from previous studies (Walton et al. 2015; Sun et al. 2015; Berg et al. 2015), we apply the validated statistical model to downscale regional snowfall and snowpack changes corresponding to all available GCMs. We further downscale GCM output for the end-of-century time slice (2081–2100) under both the "business-as-usual" RCP8.5 scenario and the "mitigation" RCP 2.6 scenario to assess snow changes associated with different emissions scenarios and time periods.

We project that in the future, the Southern California mountains are likely to receive substantially less snowfall and have less snowpack on the ground than in the baseline period. Under RCP8.5, mid-century area-mean snowfall is just 70% of the corresponding baseline value. Under RCP2.6, the amount is somewhat higher (80% of baseline snowfall). After mid-century, however, the two scenarios diverge significantly. By end-of-century under RCP8.5, snowfall sees a dramatic further reduction from mid-century levels; area-mean snowfall is only about half the baseline value. On the other hand, under RCP2.6 snowfall sees only a minimal further reduction from mid-century values. Due to the spread in the GCM climate projections, these values are all associated with large inter-model uncertainty, in the range of 50–60 percentage points. For both time slices, the snowfall loss is consistently greatest at low and moderate elevations. At higher elevations, snowfall totals are similar to those in the baseline, and about one-third of GCMs project a snowfall increase. High-elevation snowfall is insensitive to warming because temperatures are well below the freezing point of water. Instead, its changes are dominated by total precipitation change.

We project that the percentage reduction of snowpack, represented by April 1st SWE, is larger than that of snowfall, especially at low and moderate elevations. The difference between winter snowfall reductions and April 1st SWE reductions is about15–20 percentage points at low and moderate elevations for both periods and both scenarios. In addition to its impacts on winter snow accumulation, warming further enhances snowmelt at these elevations. However, the further reduction is only a few percentage points at high elevations. For low and moderate elevations, about two-thirds of the April 1st SWE loss is due to snowfall reduction, while about one-third is due to enhanced melting. The greater percentage snowfall and snowpack loss at low and moderate elevations in all future climate states probably accounts for the variation in snowfall and snowpack loss across the region's mountain complexes, which vary in their average elevations.

The effect of snowfall decline on streamflow from mountain snow will be magnified by warming-accelerated melting. A comprehensive assessment of the effect of snowmelt changes on streamflow in the region is beyond the scope of this study. However, it is possible to make meaningful inferences based on simulated snowpack from the dynamically downscaled baseline and mid-century climate under RCP8.5. Fig.

11a presents the date when the ground becomes snow-free in the baseline. This snow-free date is defined as the day when SWE reaches a critically low value. A subjective value of 2mm is used here, though the results are not sensitive to this threshold. The spatial distribution of the snow-free date matches the snowfall distribution. On mountain peaks, the seasonal snow cover disappears from the landscape after June 1, while at lower elevations, snow cover disappears as early as February. Figs. 11b–f show that in all five mid-century dynamical simulations, the dates on which snow completely disappears generally occurs earlier than during the baseline period. A spread is evident among the GCMs in how much earlier the snow-free dates occur. On average, the snow-free date occurs 16 days earlier. For each GCM, snowmelt timing is sensitive to winter and spring temperature, with the greatest changes apparent at low elevations, where winter and spring temperatures are warmer. In contrast, significantly earlier snow-free dates are not seen at high elevations, where warming likely has limited impact on snowfall or snowmelt.

Our projections reveal how the stark contrast between the global warming outcomes of the two emissions scenarios by century’s end corresponds to a dramatic difference in snowfall and snowpack outcomes in the mountains of Southern California. From our projections, it is clear that roughly one-third of snowfall and a somewhat greater amount of snowpack are likely to be lost by mid-century, no matter how aggressively greenhouse gas emissions are reduced. By end-of-century, however, the choice of emissions scenario does make a difference. The amount of snowfall likely to be lost at end-of-century (roughly half of baseline snowfall), and the corresponding further reduction of the snowpack, can be substantially mitigated by aggressively reducing greenhouse gas emissions in the coming decades.

Acknowledgments

Support for this work was provided by the City of Los Angeles and the US Department of Energy as part of the American Recovery and Reinvestment Act of 2009. Additional funding was provided by the National Science Foundation (Grant #EF-1065863, "Collaborative Research: Do Microenvironments Govern Macroecology?") and the Southwest Climate Science Center.

References:

Abatzoglou J. T., 2011: Influence of the PNA on declining mountain snowpack in the western United States. International Journal of Climatology 31: 1135–1142

Ashfaq, M., S. Ghosh, S.-C. Kao, L. C. Bowling, P. Mote, D. Touma, S. A. Rauscher, and N. S. Diffenbaugh, 2013: Near-term acceleration of hydroclimatic change in the western U.S.. J. Geophys. Res.: Atmospheres 118, 10,676-10,693.

Bales, R. C., N. P. Molotch, T. H. Painter, M. D. Dettinger, R. Rice, and J. Dozier, 2006: Mountain hydrology of the western United States. Water Resour. Res., 42, W08432, doi:10.1029/ 2005WR004387.

Barnett, T. P., J. C. Adam, and D. P. Lettenmaier, 2005: Potential impacts of a warming climate on water availability in snow- dominated regions. Nature, 438, 303–309.

Barnett, T. P., and Coauthors, 2008: Human-induced changes in the hydrology of the western United States. Science, 319, 1080–1083, doi:10.1126/science.1152538.

Baxter, M. A., C. E. Graves, and J. T. Moore, 2005: A climatology of snow-to-liquid ratio for the contiguous United States. Wea. Forecasting, 20, 729–744.

Berg N., A. Hall, F. Sun, S. Capps, D. Walton, B. Langenbrunner, and J.D. Neelin, 2015: Twenty-First-Century Precipitation Changes over the Los Angeles Region. J. Climate, 28, 401–421.

Brovkin, V., L. Boysen, T. Raddatz, V. Gayler, A. Loew and M. Claussen, 2013: Evaluation of vegetation cover and land-surface albedo in MPI-ESM CMIP5 simulations. Journal of Advances in Modeling Earth Systems, 5, 48-57. doi:10.1029/2012MS000169

Caldwell P., H.N.S. Chin, D.C. Bader, and G. Bala, 2009: Evaluation of a WRF dynamical downscaling simulation over California. Climatic Change, 95, 499–521.

Cayan D.R., 1996: Interannual climate variability and snowpack in the western United States, J. Climate, 9, 928-948.

Cayan, D.R, S. Kammerdiener, M.D. Dettinger, J.M. Caprio, and D.H. Peterson. 2001: Changes in the onset of spring in the western United States. Bull. Amer. Meteor. Soc., 82: 399–415.

Cayan, D.R., E.P. Maurer, M.D. Dettinger, M. Tyree and K. Hayhoe, 2008: Climate change scenarios for the California region. Climatic Change, 87, 21–42.

Chen, F., and J. Dudhia, 2001: Coupling an advanced land surface–hydrology model with the Penn State–NCAR MM5 modeling system. Part I: Model implementation and sensitivity. Mon. Wea. Rev., 129, 569–585.

Chin H.S., 2008: Dynamical downscaling of GCM simulations: toward the improvement of fore-cast bias over California. LLNL-TR-407576, Lawrence Livermore National Lab. https://e-reports-int.llnl.gov/pdf/365755.pdf, 16pp.

Donner, L. J. and coauthors, 2012: The dynamical core, physical parameterizations, and basic characteristics of the atmospheric component AM3 of the GFDL global coupled model CM3. Journal of Climate, 24, 3484–3519.

Dudhia, J., 1989: Numerical study of convection observed during the winter monsoon experiment using a mesoscale two-dimensional model. J. Atmos. Sci., 46, 3077–3107.

Gent, P. R., and coauthors, 2011: The Community Climate System Model version 4. J. Climate, 24, 4973–4991.

Giorgi, F., B. Hewitson, J. Christensen, M. Hulme, H. von Storch, P.Whetton, R. Jones, L. Mearns and C. Fu, 2001: Regional climate information-evaluation and projections. In: J.T. Houghton, Y. Ding, D.J. Griggs, M. Noguer, P.J. van der Linden, X. Dai, K. Maskell and C.A. Johnson (eds.). pp. 583–638. Climate Change 2001: The Scientific Basis. Contribution of Working Group I to the Third Assessment Report of the Intergovernmental Panel on Climate Change. Cambridge University Press.

Hamlet, A. F., P. W. Mote, M. P. Clark, and D. P. Lettenmaier. 2005. Effects of temperature and precipitation variability on snowpack trends in the western United States. Journal of Climate 18:4545-4561.

Hara, M., T. Yoshikane, H. Kawase, and F. Kimura, 2008: Estimation of the impact of global warming on snow depth in Japan by the pseudo-global-warming method. Hydrol. Res. Lett., 2, 61–64.

Hayhoe, K, Cayan D, Field CB, Frumhoff PC, 2004: Emissions pathways, climate change, and impacts on California. Proc. Nat. Acad. Sci. 101:12422–12427

Hong, S. Y., and J. O. J. Lim, 2006: The WRF single-moment 6-class microphysics scheme (WSM6). J. Korean Meteor. Soc, 42, 129–151.

Howat, I. M., and S. Tulaczyk, 2005: Climate sensitivity of spring snowpack in the Sierra Nevada. J. Geophys. Res., 110, F04021, doi:10.1029/2005JF000356

Judson, A. and N. Doesken, 2000: Density of Freshly Fallen Snow in the Central Rocky Mountains. Bull. Amer. Meteor. Soc., 81, 1577–1587.

Kain, J, S., 2004: The Kain–Fritsch convective parameterization: An update. J. Appl. Meteor. Soc., 43, 170–181.

Kapnick, S, Hall A, 2010: Observed climate-snowpack relationships in California and their implications for the future. J. Climate, 23: 3446-3456, DOI:10.1175/2010JCLI203.1

Kapnick, S. and Hall A., 2012: Causes of recent changes in western North American snowpack. Clim. Dyn. 38, 1885-1899, doi: 10.1007/s00382-011-1089-y

Kawase, H., T. Yoshikane, M. Hara, F. Kimura, T. Yasunari, B. Ailikun, H. Ueda, and T. Inoue, 2009: Intermodel variability of future changes in the Baiu rainband estimated by the pseudo global warming downscaling method. J. Geophys. Res., 114, D24110, doi:10.1029/2009JD011803

Kay, J. E., 2006: Snow density observations in the Washington Cascades. Proceedings of the 74th Western Snow Conference, Las Cruces, NM, 12 pp.

Kim, J., T. Kim, R. W. Arritt, and N. L. Miller, 2002: Impacts of increased atmospheric CO2 on the hydroclimate of the western United States. J. Climate, 15, 1926–1942.

Klos, P.Z., T.E. Link and J.T. Abatzoglou, 2014: Extent of the rain-snow transition zone in the western U.S. under historic and projected climate, Geophy. Res. Lett., 41, doi:10.1002/2014GL060500.

Knowles, N., and D. R. Cayan, 2002: Potential effects of global warming on the Sacramento/San Joaquin watershed and the San Francisco estuary. Geophys. Res. Lett., 29(18), 1891, doi:10.1029/2001GL014339.

Knowles N., Dettinger M.D., and Cayan D., 2006: Trends in Snowfall versus Rainfall in the Western United States. J. Climate, 19, 4545–4559.

Knutsen, T. R., J. J. Sirutus, S. T. Garner, G. A. Vecchi, and I. M. Held, 2008: Simulated reduction in Atlantic hurricane frequency under twenty-first century warming conditions. Nat. Geosci., 1, 359¬–364.

Lauer, A., K. Hamilton, Y. Wang, V. T. J. Phillips, and R. Bennartz, 2010: The impact of global warming on marine boundary layer clouds over the eastern Pacific—A regional model study. J. Climate, 23, 5844–5863.

Leung L.R., and S.J. Ghan, 1999: Pacific Northwest Sensitivity Simulated by a Regional Climate Model Driven by a GCM. Part II: 2XCO2 Simulations, J. Climate, 12, 2031–2053.

Leung, L. R., and Y. Qian, 2003: The sensitivity of precipitation and snowpack simulations to model resolution via nesting in regions of complex terrain. J. Hydrometeor., 4, 1025–1043.

Leung L.R., Y. Qian, and X. Bian, 2003: Hydroclimate of the western United States based on observations and regional climate simulations of 1981–2000. Part I: seasonal statistics. J. Climate, 16, 1892–1911.

Leung, L R, Y. Qian, X. Bian, W. M. Washington, J. Han, and J. O. Roads, 2004: Mid-century ensemble regional climate change scenarios for the western United States. Climatic Change, 62, 75–113.

Lin, Y.-L., R. D. Farley, and H. D. Orville, 1983: Bulk parameterization of the snow field in a cloud model. J. Climate Appl. Meteor., 22, 1065–1092.

Luce, C. H., J. T. Abatzoglou, and Z. A. Holden, 2013: The missing mountain water: Slower westerlies decrease orographic enhancement in the Pacific Northwest USA, Science, 342(6164), 1360–1364, doi:10.1126/science.1242335.

Maurer, E.P., 2007: Uncertainty in hydrologic impacts of climate change in the Sierra Nevada, California under two emissions scenarios, Climatic Change, Vol. 82, No. 3-4, 309-325, doi: 10.1007/s10584-006-9180-9

Meinshausen, M., S. J. Smith, K. V. Calvin, J. S. Daniel, M. Kainuma, J.-F. Lamarque, K. Matsumoto, S. A. Montzka, S. C. B. Raper, K. Riahi, A. M. Thomson, G. J. M. Velders and D. van Vuuren, 2011: The RCP greenhouse gas concentrations and their extension from 1765 to 2300. Climatic Change (Special Issue), DOI:10.1007/s10584

Mesinger, F., G. DiMego, E. Kalnay, K. Mitchell, P.C. Shafran, W. Ebisuzaki, and W. Shi, 2006: North American regional reanalysis. Bull. Amer. Meteor. Soc., 87(3), 343–360.

Minder J., 2010: The Sensitivity of Mountain Snowpack Accumulation to Climate Warming. J. Climate, 23, 2634–2650.

Mlawer, E. J., S. J., Taubman, P. D. Brown, M. J. Iacono, and S. A. Clough, 1997: Radiative transfer for inhomogeneous atmospheres: RRTM, a validated correlated-k model for the longwave, J. Geophys. Res.: Atmospheres (1984–2012), 102(D14), 16663–16682.

Mote, P. W., 2003: Trends in SWE in the Pacific Northwest and their climatic causes. Geophy. Res. Lett., 30(12), doi: 10.1029/2003GL017258

Mote P., 2006: Climate-driven variability and trends in mountain snowpack in Western North America. J Climate, 19, 6209–6220.

Mote P., A. Hamlet, M. Clark, and D. Lettenmaier, 2005: Declining mountain snowpack in Western North America. Bull. Amer. Meteor. Soc., 86, 39–40.

Pan, L.-L., S.-H. Chen, D. Cayan, M.-Y. Lin, Q. Hart, M.-H. Zhang, Y. Liu, and J. Wang, 2011: Influences of climate change on California and Nevada regions revealed by a high-resolution dynamical downscaling study. Clim. Dyn., 37, 2005–2020.

Pavelsky, T. M., S. Kapnick, and A. Hall, 2011: Accumulation and melt dynamics of snowpack from a multiresolution regional climate model in the central Sierra Nevada, California. J. Geophys. Res., 116, D16115, doi:10.1029/2010JD015479

Pederson, G. T., S. T. Gray, C. A. Woodhouse, J. L. Betancourt, D. B. Fagre, J. S. Littell, E. Watson, B. H. Luckman, and L. J. Graumlich, 2011: The unusual nature of recent snowpack declines in the North American cordillera, Sciencexpress, doi:10.1126/science.1201570.

Pierce, D., and D. Cayan, 2013: The uneven response of different snow measures to human-induced climate warming. J. Climate, 26, 4148–4167.

Pierce, D., and Coauthors, 2013: Probabilistic estimates of future changes in California temperature and precipitation using statistical and dynamical downscaling. Clim. Dyn., 40, 836– 856, doi:10.1007/s00382-012-1337-9.

Pomeroy, J.W. and E. Brun, 2001: Physical properties of snow. In Snow Ecology: an Interdisciplinary Examination of Snow-covered Ecosystems (eds. H.G. Jones, J.W. Pomeroy, D.A. Walker and R.W. Hoham). Cambridge University Press, Cambridge, UK, 45–118.

Qian, Y., S.J. Ghan, and L.R. Leung, 2009: Downscaling hydroclimatic changes over the Western U.S. Based on CAM subgrid scheme and WRF regional climate simulations. Int. J. Climatol., 30, 675–693.

Rasmussen, R., C. Liu, K. Ikeda, D. Gochis, D. Yates, F. Chen, and E. Gutmann, 2011: High-resolution coupled climate runoff simulations of seasonal snowfall over Colorado: A process study of current and warmer climate. J. Climate, 24(12), 3015–3048.

Roebber P.J., S.L. Bruening, D.M. Schultz, and J.V. Cortinas, 2003.: Improving snowfall forecasting by diagnosing snow density. Weather and Forecasting, 18(2), 264–287.

Salathé, E., R. Steed, C. Mass, and P. H. Zahn, 2008: A high-resolution climate model for the U.S. Pacific Northwest: Mesoscale feedbacks and local responses to climate change. J. Climate, 21, 5708–5726.

Sato, T., F. Kimura, and A. Kitoh, 2007: Projection of global warming onto regional precipitation over Mongolia using a regional climate model. J. Hydrol., 333, 144–154.

Schär, C., C. Frei, D. Lüthi, and H. C. Davies, 1996: Surrogate climate-change scenarios for regional climate models. Geophys. Res. Lett., **23**(6), 669–672. doi:10.1029/96GL00265.

Seo, H., and S.-P. Xie, 2011: Response and impact of equatorial ocean dynamics and tropical instability waves in the tropical Atlantic under global warming: A regional coupled downscaling study. J. Geophys. Res., 116, C03026. doi:10.1029/2010JC006670.

Serreze, M.C., M.P. Clark, R.L. Armstrong, D.A. McGinnis and R.S. Pulwarty, 1999: Characteristics of the western United States snowpack from snowpack telemetry (SNOTEL) data. Water Resour. Res., 35(7), 2145–2160.

Skamarock W. C., J. B. Klemp, J. Dudhia, D. O. Gill, D. M. Barker, M. G. Duda, X.-Y. Huang, W. Wang, and J. G. Powers, 2008: A description of the Advanced Research WRF Version 3. NCAR Tech. Note NCAR/TN-475+STR, June 2008, 125 pp.

Snyder, M. A., L. C. Sloan, and J. L. Bell, 2004: Modeled regional climate change in the hydrologic regions of California: A CO2 sensitivity study. J. Am. Water Resour. Assoc., 40, 591–601.

Sun F., D. Walton, and A. Hall, 2015: A hybrid dynamical–statistical downscaling technique, part II: End-of-century warming projections predict a new climate state in the Los Angeles region. J. Climate, in press.

Taylor, K. E., R. J. Stouffer, and G. A. Meehl, 2012: An overview of CMIP5 and the experiment design, Bull. Amer. Meteor. Soc., 93, 485–498.

Voldoire, A. and coauthors, 2012: The CNRM-CM5.1 global climate model: description and basic evaluation. Clim. Dyn., 1–31, 10.1007/s00382-011-1259-y.

von Storch, H., E. Zorita and U. Cubasch, 1993: Downscaling of global climate change estimates to regional scales: An application to Iberian rainfall in wintertime. J. Climate, 6,1161–1171.

Walton D., F. Sun, A. Hall, and S. Capps, 2015: A hybrid dynamical–statistical downscaling technique, part I: Development and validation of the technique. J. Climate, in press.

Wang Y., L.R. Leung, J.L. McGregor, D.K. Lee, W.C. Wang, Y. Ding , and F. Kimura, 2004: Regional climate modeling: progress, challenges, and prospects. J. Meteor. Soc. Japan., 82, 1599–1628.

Watanabe, S. and coauthors, 2011: MIROC-ESM: model description and basic results of CMIP5-20c3m experiments. Geosci. Model Dev. Discuss, 4,1063–1128.

Wilby, R.L., S.P. Charles, E. Zorita, B. Timbal, P. Whetton, L.O. Mearns, 2004: Guidelines for use of climate scenarios developed from statistical downscaling methods: supporting material of the Intergovernmental Panel on Climate Change, Task Group on Data and Scenario Support for Impacts and Climate Analysis, Rotherham.

List of Tables

TABLE 1: Summary of information associated with observational stations from National Weather Service (NWS) Cooperative Observer Program (COOP) used to validate the baseline simulation.

Station Name	NWS COOP ID	Latitude	Longitude	Elevation (meter)	Elevation in WRF (meter)	Observational Period
Big Bear Lake	040741	34’15’’	116’53’’	2070	2096	1960/07-2005/12
Lake Arrowhead	044671	34’15’’	117’11’’	1587	1566	1941/08-2011/11
Idyllwild	044211	33’45’’	116’43’’	1644	1630	1943/10-2012/09
Tehachapi	048826	35’08’’	118’27’’	1224	1258	1893/01-1997/06

TABLE 2: Name and identifying information (country, institution) of the CMIP5 GCMs used for downscaling in this study. Check marks indicate which emissions scenarios are used. All GCMs are statistically downscaled using the hybrid method, whereas only CCSM4, GFDL-CM3, CNRM-CM5, MIROC-ESM-CHEM, and MPI-ESM-LR (highlighted in bold) are dynamically downscaled.

MODEL	COUNTRY	INSTITUTE	RCP2.6	RCP8.5
ACCESS1.0	Australia	Commonwealth Scientific and Industrial Research Organization		✓
ACCESS1.3	Australia	Commonwealth Scientific and Industrial Research Organization		✓
BCC-CSM1.1	China	Beijing Climate Center, China Meteorological Administration	✓	✓
BNU-ESM	China	College of Global Change and Earth System Science, Beijing Normal University		✓
Can-ESM2	Canada	Canadian Centre for Climate Modelling and Analysis	✓	✓
CCSM4	**USA**	**National Center for Atmospheric Research**	✓	✓
CESM1(BGC)	USA	National Science Foundation, Department of Energy, National Center for Atmospheric Research		✓
CESM1(CAM5)	USA	National Science Foundation, Department of Energy, National Center for Atmospheric Research	✓	✓
CMCC-CM	Italy	Centro Euro-Mediterraneo per I Cambiamenti Climatici		✓
CNRM-CM5	**France**	**Centre National de Recherches Meteorologiques**	✓	✓
CSIRO-Mk3.6.0	Australia	Commonwealth Scientific and Industrial Research Organization	✓	✓
EC-EARTH	Europe	EC-Earth Consortium		✓
GFDL-CM3	**USA**	**NOAA Geophysical Fluid Dynamics Laboratory**	✓	✓
GFDL-ESM2M	USA	NOAA Geophysical Fluid Dynamics Laboratory		✓
GFDL-ESM2G	USA	NOAA Geophysical Fluid Dynamics Laboratory	✓	✓
GISS-E2-H	USA	NASA Goddard Institute for Space Studies	✓	✓
GISS-E2-R	USA	NASA Goddard Institute for Space Studies	✓	✓
HadGEM2-AO	UK	Met Office Hadley Centre	✓	✓
HadGEM2-CC	UK	Met Office Hadley Centre		✓
HadGEM2-ES	UK	Met Office Hadley Centre	✓	✓
INMCM4	Russia	Institute for Numerical Mathematics		✓
IPSL-CM5A-LR	France	Institut Pierre Simon Laplace	✓	✓
IPSL-CM5A-MR	France	Institut Pierre Simon Laplace	✓	✓
MIROC-ESM	Japan	AORI (U. Tokyo), NIES, JAMESTEC	✓	✓
MIROC-ESM-	**Japan**	**AORI (U. Tokyo), NIES,**	✓	✓

CHEM		**JAMESTEC**		
MIROC5	Japan	AORI (U. Tokyo), NIES, JAMESTEC	✓	✓
MPI-ESM-LR	**Germany**	**Max Planck Institute for Meteorology**	✓	✓
MRI-CGCM3	Japan	Meteorological Research Institute	✓	✓
NorESM1-M	Norway	Norwegian Climate Center	✓	✓

List of Figures

Fig. 1: Topography (unit: m) of the innermost domain, shown in color at the domain's 2-km resolution. The border of Los Angeles County is also shown. Red dots represent point measurement sites, whose observations are used to validate the dynamically downscaled baseline climate simulation. Prominent mountain ranges within the model domain are also shown.

Fig. 2: Simulated baseline (1981–2000) monthly snowfall water equivalent, unit: mm) climatology for the months of November through April. Topography contour lines at 1000, 2000, and 3000 meters are highlighted. The border of Los Angeles County is shown in black.

Fig. 3: Scatter plots between observed and WRF simulated snowfall water equivalent, unit: mm) at four sites: Tehachapi, Idyllwild, Lake Arrowhead, and Big Bear Lake. Left panel: baseline period (1981–2000) monthly snowfall climatology; Right panel: annual accumulated snowfall.

Fig. 4: Correlations between snowfall at each elevation bin (every 100 m) in each winter month (DJFM) and precipitation (x-direction) and temperature (y-direction) of the same month for the baseline period (1981–2000). The reference arrow in the upper right corner indicates a correlation of 1.0 in each direction. Significantly positive correlations with precipitation are expected in each elevation bin, especially in high elevations.

Significantly negative correlations with temperature are seen in low- to mid-elevation bins.

Fig. 5: Scatterplots of the WRF-simulated and statistically downscaled snowfall water equivalent (unit: mm) in each February of the baseline period (1981–2000) for three binned elevations: (a) 2500–2600 m, (b) 2000–2100 m, and (c) 1500–1600 m. The interannual correlation coefficients between statistically downscaled and WRF-simulated snowfall are noted.

Fig. 6: Seasonal cycles of snowfall water equivalent (unit: mm) for elevations above 1500 meters. Shown are results from the dynamically downscaled baseline (1981–2000) period (black); the dynamically downscaled projections (red) in mid-century (2041– 2060); and the corresponding mid-century statistically downscaled projections (green).

Fig. 7: Winter (DJFM) accumulated snowfall water equivalent (unit: mm) for five WRF-GCM simulations as a function of elevation (binned by each 100 m). All grid cells are binned in 100-m increments, and then the average accumulated snowfall (DJFM) is calculated for each elevation bin. Shown are the dynamically downscaled baseline (1981–2000) simulation (black); dynamically downscaled mid-century (2041–2060) projections (red); and corresponding statistically downscaled mid-century projections (green).

Fig. 8: As in Fig. 7, but for April 1st snow water equivalent projections.

Fig. 9: Box and whisker plots of projected winter (DJFM) accumulated snowfall water equivalent (SFE) and April 1^{st} snow water equivalent (SWE) under RCP8.5, as a percentage of baseline (1981–2000) values and as a function of the elevation (binned by each 100 m). Panel (a) shows mid-century (2041–2060) SFE; (b) shows end-of-century (2081–2100) SFE; (c) shows mid-century April 1^{st} SWE; and (d) shows end-of-century April 1^{st} SWE. Whiskers denote maximum and minimum values, the upper and and lower edges of the boxes denote the 75^{th} and 25th percentiles, respectively, and the band inside the box denotes the ensemble-mean. The symbol “x” denotes the ensemble-mean value corresponding to the RCP2.6 forcing scenario.

Fig. 10: Ensemble-mean mid-century (2041–2060) and end-century (2081–2100) winter (DJFM) accumulated snowfall water equivalent and April 1^{st} snow water equivalent under RCP8.5 and RCP2.6, as a percentage of baseline (1981–2000) values, for low (1500–2000 m), moderate (2000–2500 m), and high (greater than 2500 m) elevations.

Fig. 11: (a) Timing of snow-free date for the baseline (1981–2000), defined as the day when SWE at each grid cell reaches a critically low value, with 2mm used here. (b)–(f) Number of days earlier the snow-free dates occur at mid-century (2041–2060) in each dynamically downscaled simulation, compared to the baseline. On average, CCSM4 sees snow-free conditions 7 days earlier, CNRM-CM5 10 days, MPI-ESM-LR 16 days, GFDL-CM3 21 days, and MIROC-ESM-CHEM 24 days.

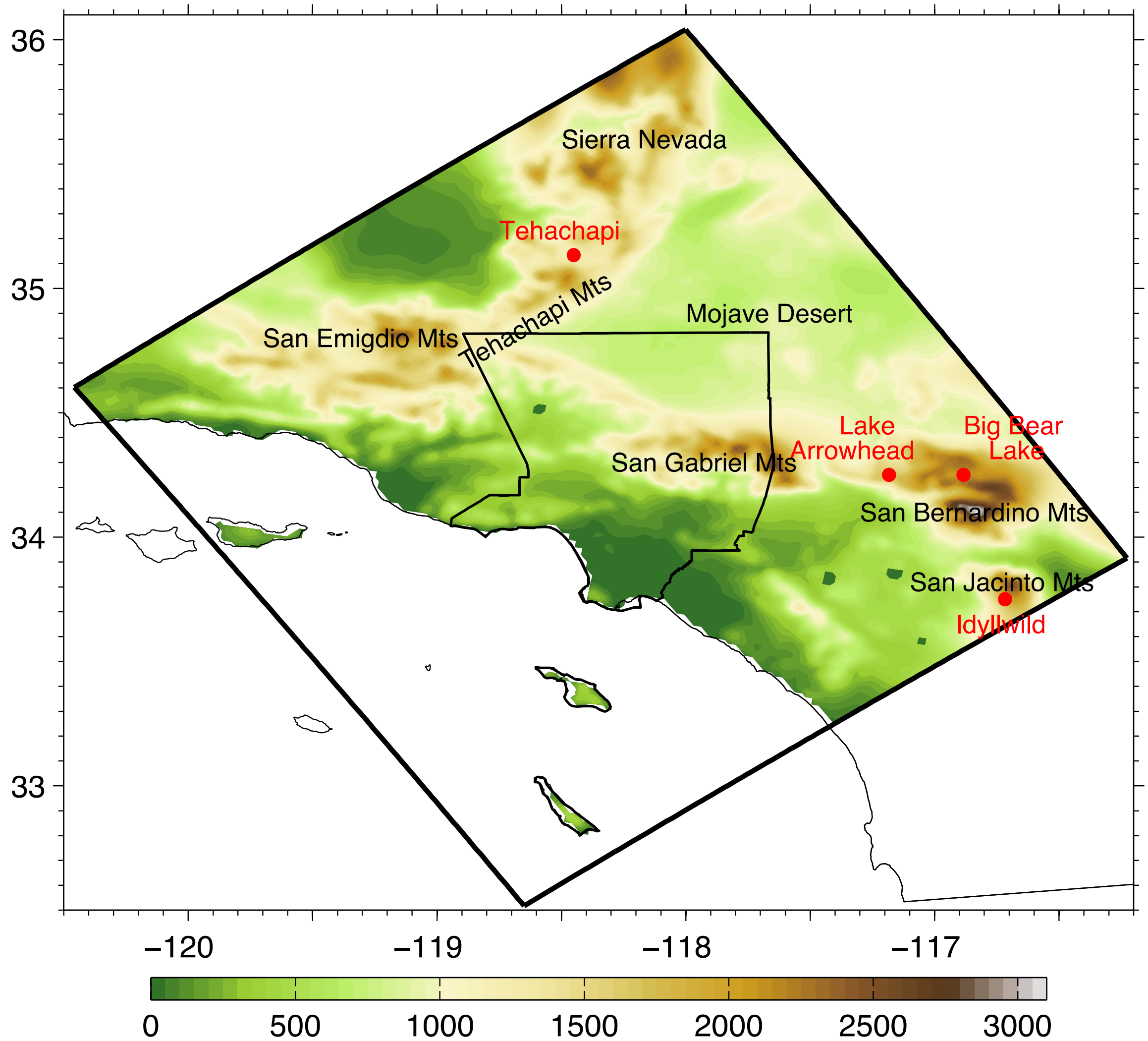

Fig. 1: Topography (unit: m) of the innermost domain, shown in color at the domain's 2-km resolution. The border of Los Angeles County is also shown. Red dots represent point measurement sites, whose observations are used to validate the dynamically downscaled baseline climate simulation. Prominent mountain ranges within the model domain are also shown.

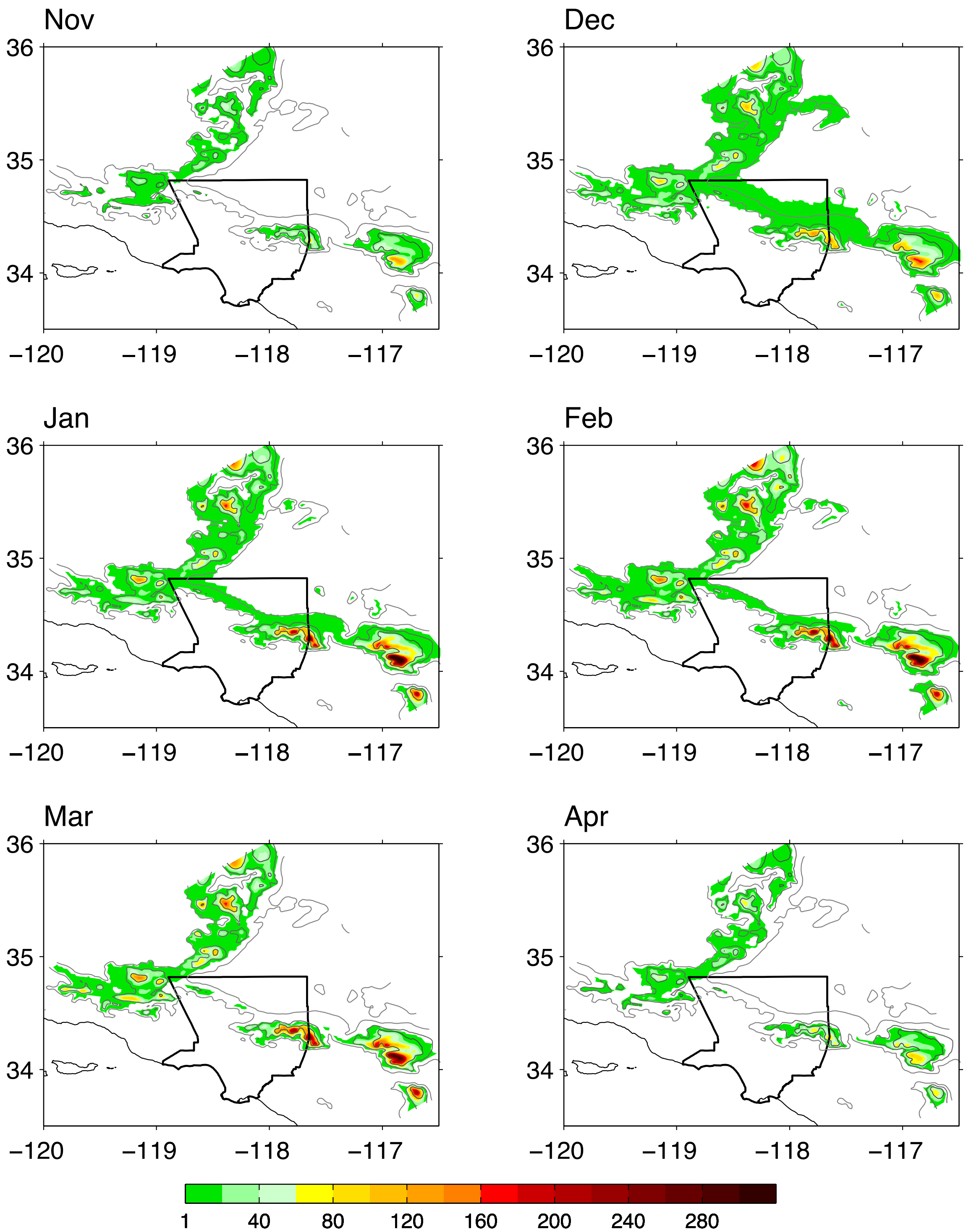

Fig. 2: Simulated baseline (1981–2000) monthly snowfall water equivalent, unit: mm) climatology for the months of November through April. Topography contour lines at 1000, 2000, and 3000 meters are highlighted. The border of Los Angeles County is shown in black.

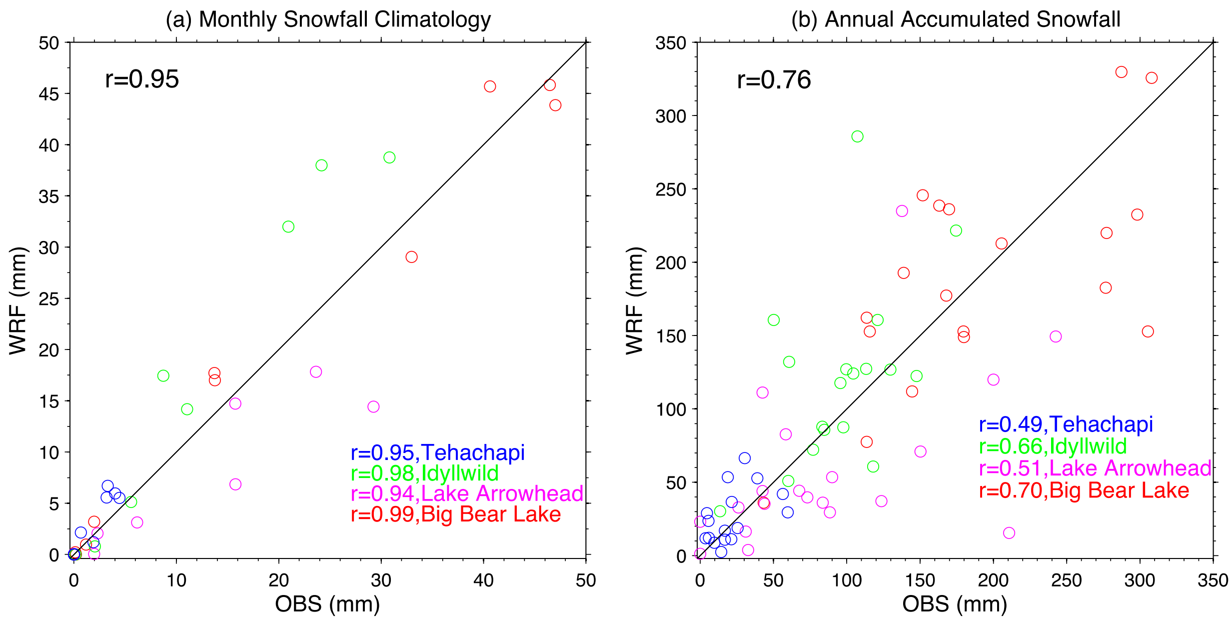

Fig. 3: Scatter plots between observed and WRF simulated snowfall water equivalent, unit: mm) at four sites: Tehachapi, Idyllwild, Lake Arrowhead, and Big Bear Lake. Left panel: baseline period (1981–2000) monthly snowfall climatology; Right panel: annual accumulated snowfall.

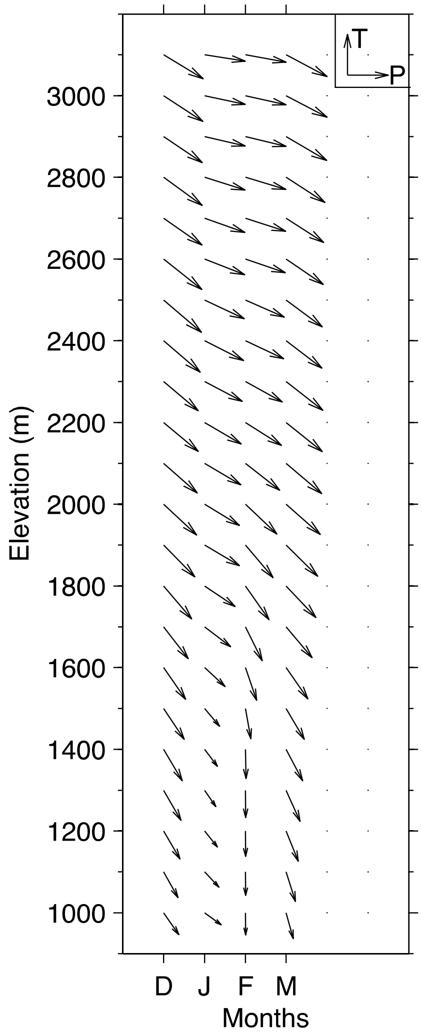

Fig. 4: Correlations between snowfall at each elevation bin (every 100 m) in each winter month (DJFM) and precipitation (x-direction) and temperature (y-direction) of the same month for the baseline period (1981–2000). The reference arrow in the upper right corner indicates a correlation of 1.0 in each direction. Significantly positive correlations with precipitation are expected in each elevation bin, especially in high elevations. Significantly negative correlations with temperature are seen in low- to mid-elevation bins.

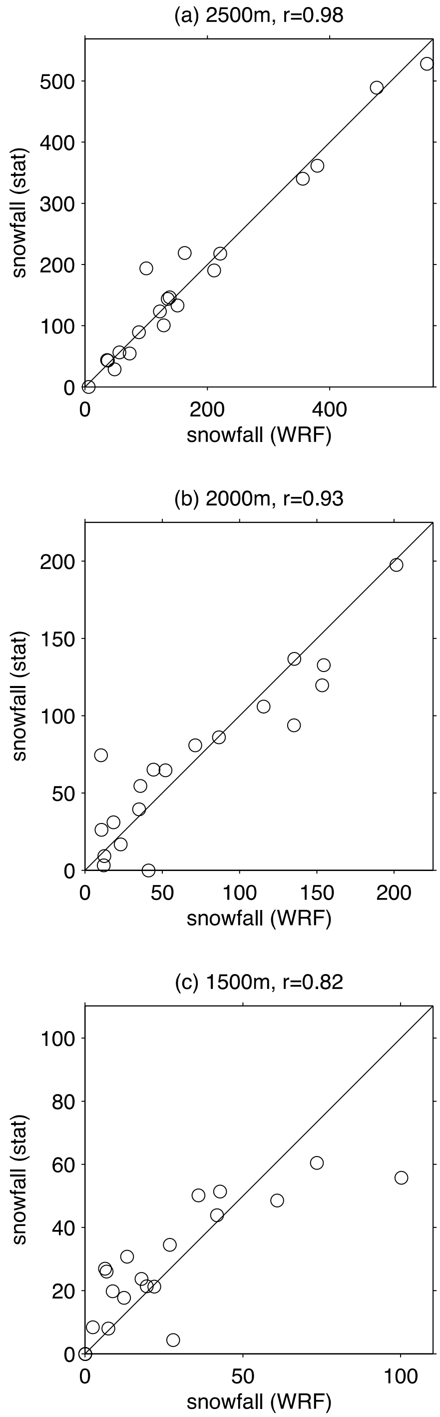

Fig. 5: Scatterplots of the WRF-simulated and statistically downscaled snowfall water equivalent (unit: mm) in each February of the baseline period (1981–2000) for three binned elevations: (a) 2500–2600 m, (b) 2000–2100 m, and (c) 1500–1600 m. The interannual correlation coefficients between statistically downscaled and WRF-simulated snowfall are noted.

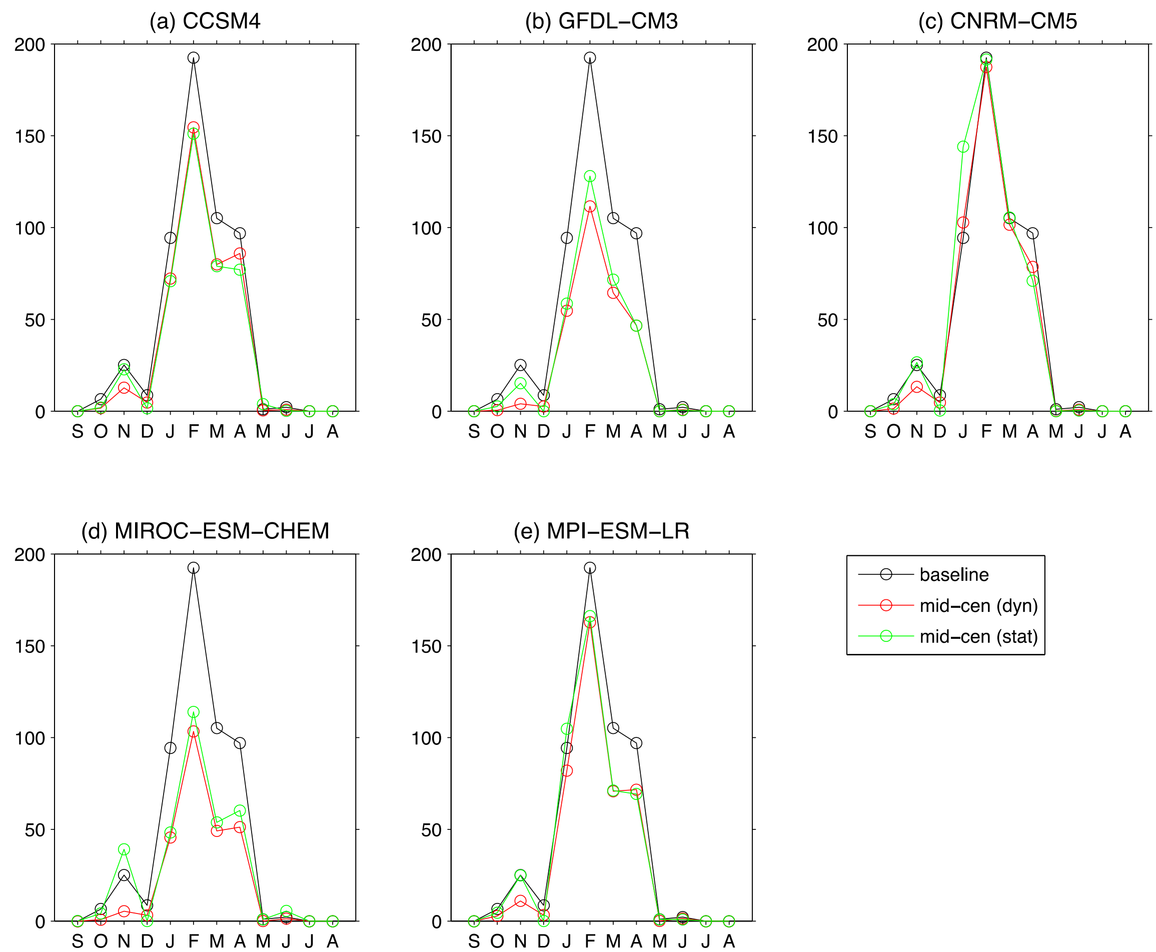

1056

1057 Fig. 6: Seasonal cycles of snowfall water equivalent (unit: mm) for elevations above 1500
1058 meters. Shown are results from the dynamically downscaled baseline (1981–2000) period
1059 (black); the dynamically downscaled projections (red) in mid-century (2041– 2060); and
1060 the corresponding mid-century statistically downscaled projections (green).
1061

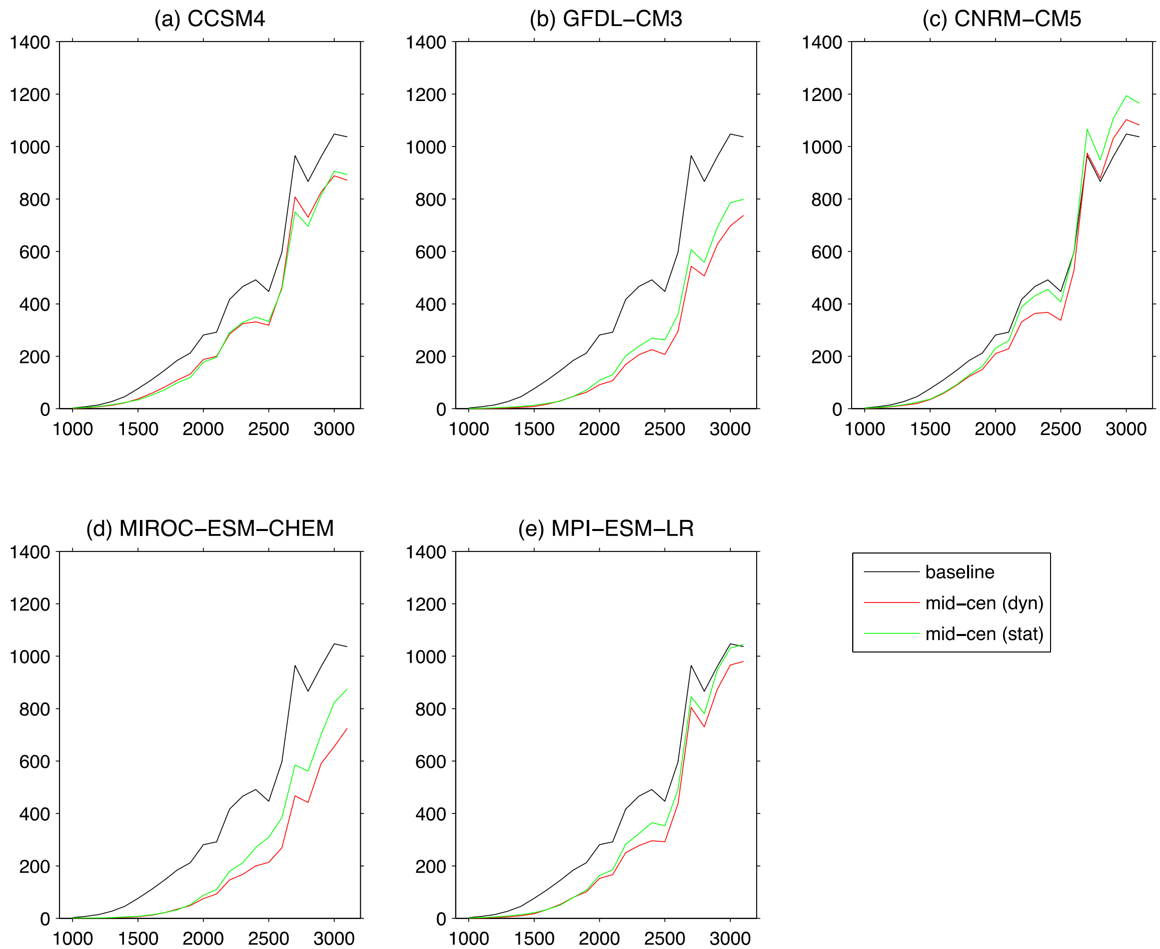

Fig. 7: Winter (DJFM) accumulated snowfall water equivalent (unit: mm) for five WRF-GCM simulations as a function of elevation (binned by each 100 m). All grid cells are binned in 100-m increments, and then the average accumulated snowfall (DJFM) is calculated for each elevation bin. Shown are the dynamically downscaled baseline (1981–2000) simulation (black); dynamically downscaled mid-century (2041–2060) projections (red); and corresponding statistically downscaled mid-century projections (green).

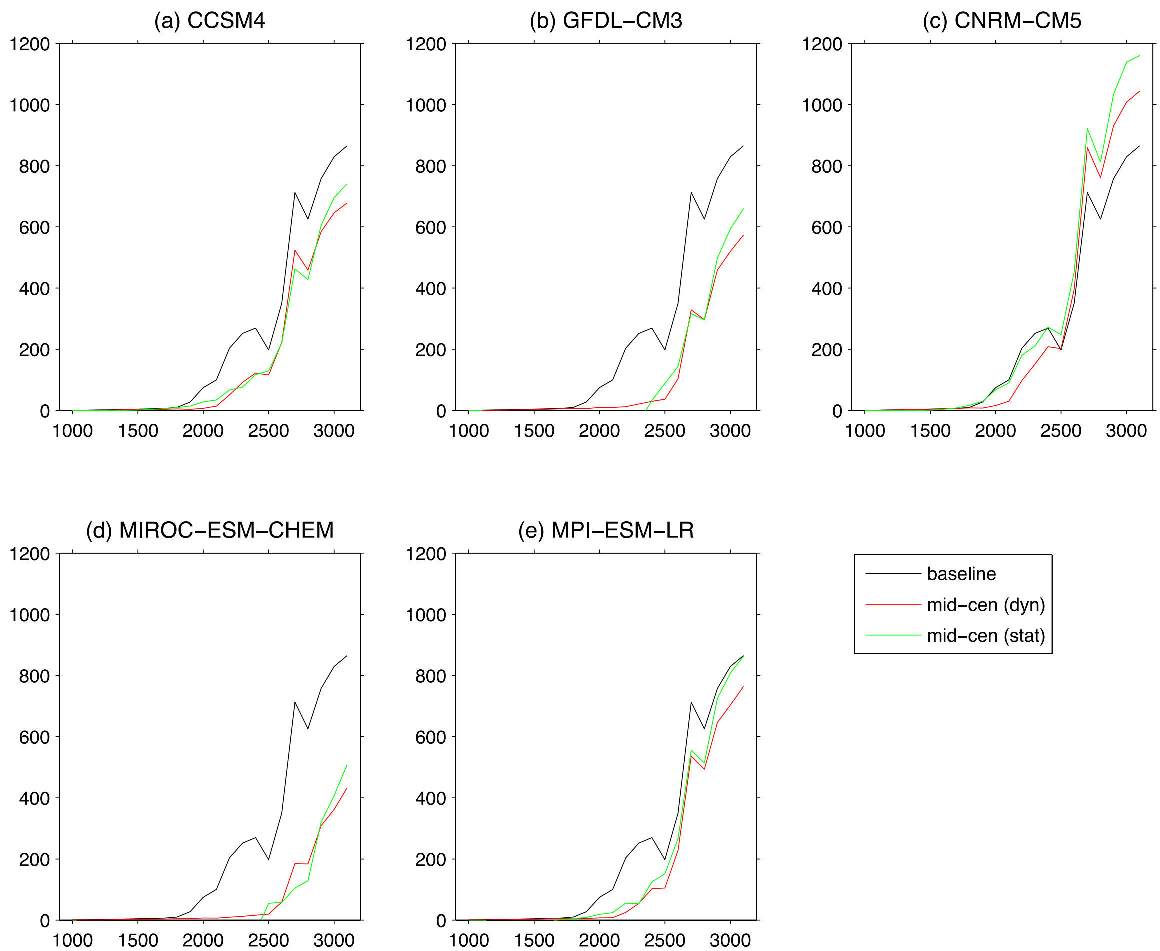

1068

1069 Fig. 8: As in Fig. 7, but for April 1st snow water equivalent projections.
1070

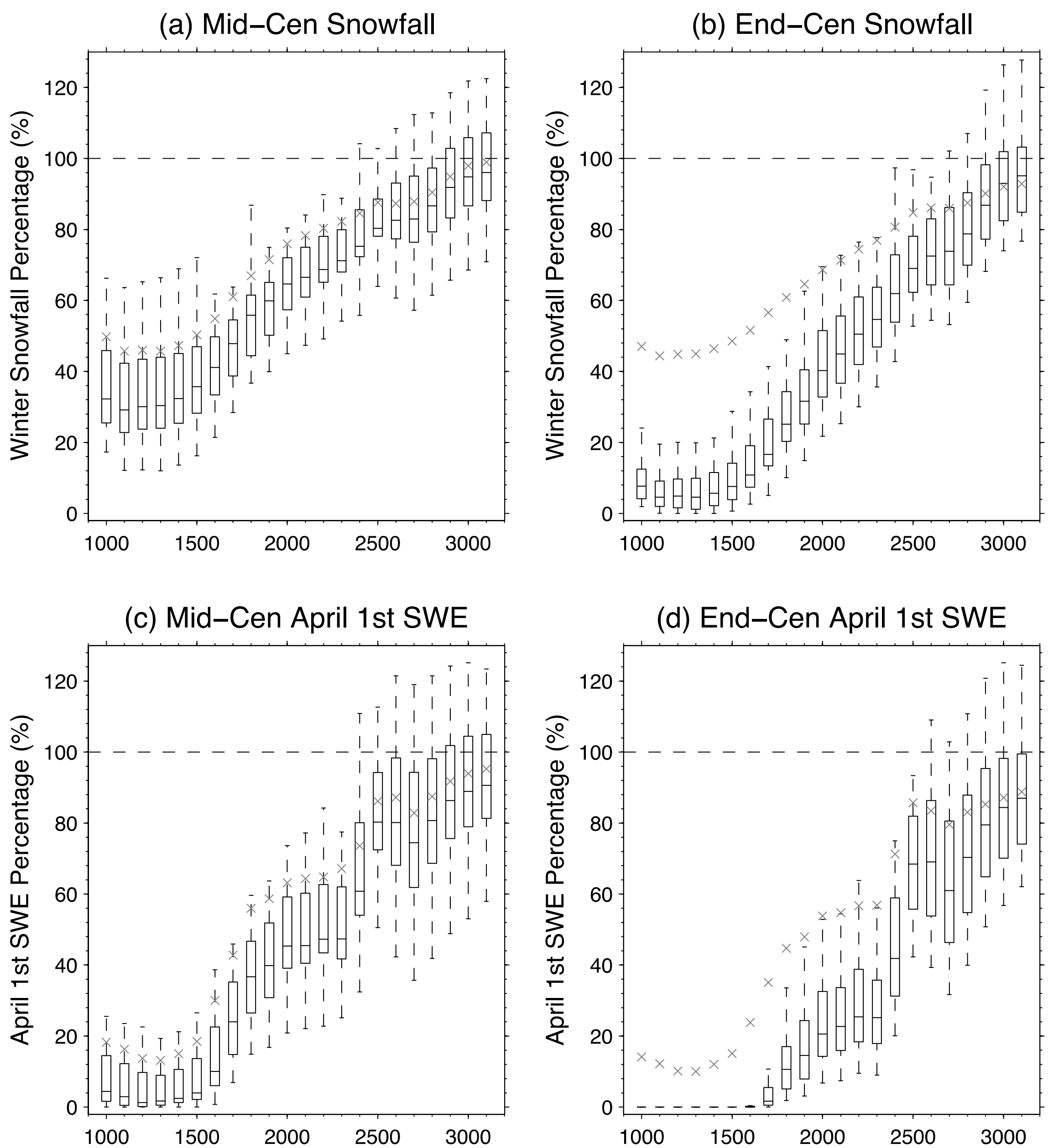

Fig. 9: Box and whisker plots of projected winter (DJFM) accumulated snowfall water equivalent (SFE) and April 1st snow water equivalent (SWE) under RCP8.5, as a percentage of baseline (1981–2000) values and as a function of the elevation (binned by each 100 m). Panel (a) shows mid-century (2041–2060) SFE; (b) shows end-of-century (2081–2100) SFE; (c) shows mid-century April 1st SWE; and (d) shows end-of-century April 1st SWE. Whiskers denote maximum and minimum values, the upper and and lower edges of the boxes denote the 75th and 25th percentiles, respectively, and the band inside the box denotes the ensemble-mean. The symbol “x” denotes the ensemble-mean value corresponding to the RCP2.6 forcing scenario.

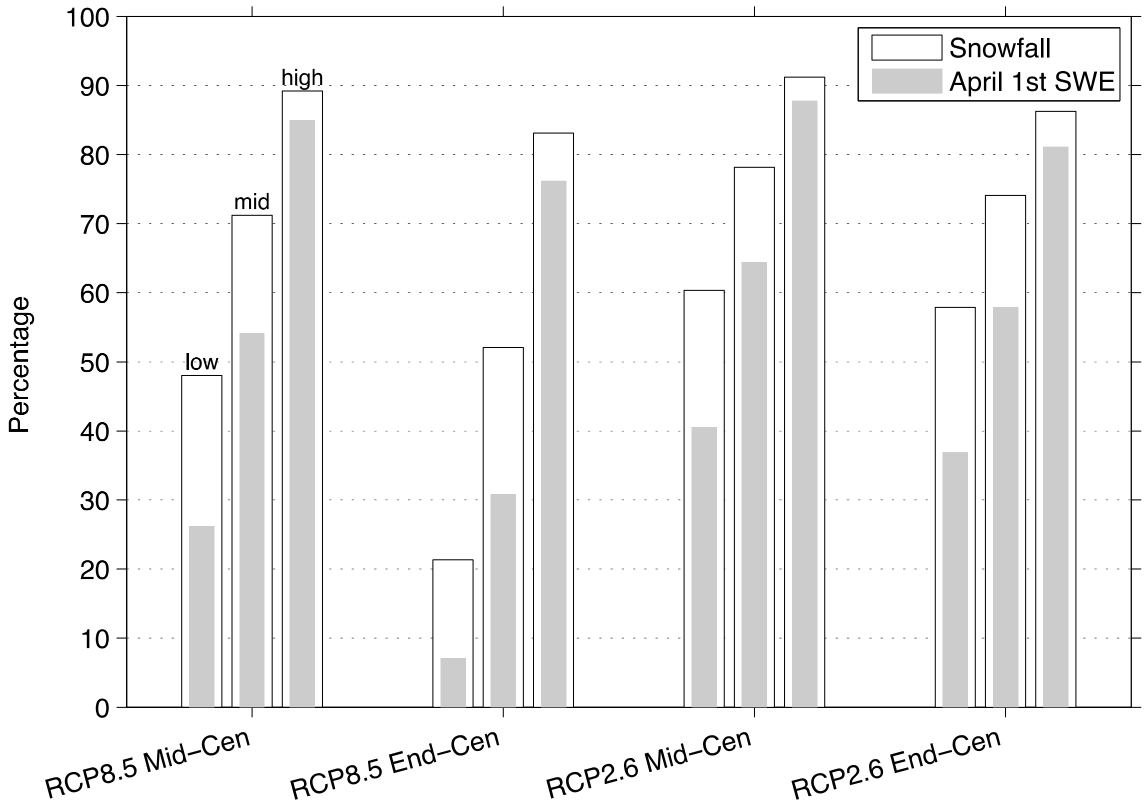

Fig. 10: Ensemble-mean mid-century (2041–2060) and end-century (2081–2100) winter (DJFM) accumulated snowfall water equivalent and April 1st snow water equivalent under RCP8.5 and RCP2.6, as a percentage of baseline (1981–2000) values, for low (1500–2000 m), moderate (2000–2500 m), and high (greater than 2500 m) elevations.

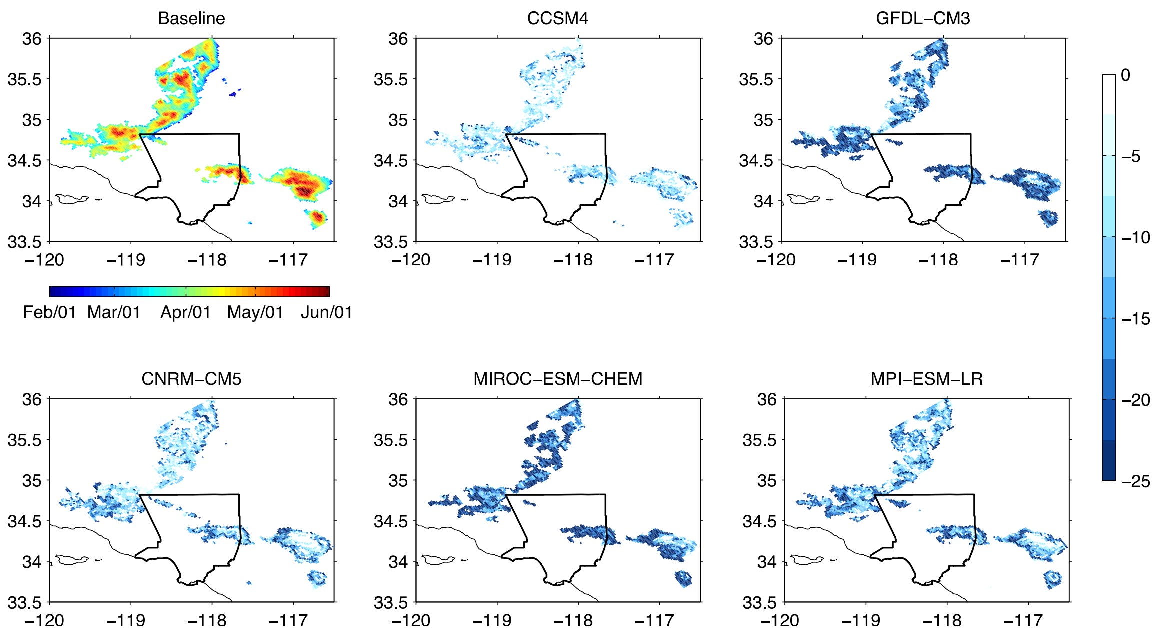

Fig. 11: (a) Timing of snow-free date for the baseline (1981–2000), defined as the day when SWE at each grid cell reaches a critically low value, with 2mm used here. (b)–(f) Number of days earlier the snow-free dates occur at mid-century (2041–2060) in each dynamically downscaled simulation, compared to the baseline. On average, CCSM4 sees snow-free conditions 7 days earlier, CNRM-CM5 10 days, MPI-ESM-LR 16 days, GFDL-CM3 21 days, and MIROC-ESM-CHEM 24 days.